Room-Temperature Switching of Perpendicular Magnetization by Magnon Torques

Guoyi Shi,[1,2,†] Fei Wang,[2,†] Hui Ru Tan,[3] Shishun Zhao,[2] Yakun Liu,[2] Dongsheng Yang,[2] Kyusup Lee,[2] Yuchen Pu,[2] Shuhan Yang,[2] Anjan Soumyanarayanan,[3,4] and Hyunsoo Yang[1,2,*]

[1]*Integrative Sciences and Engineering Programme, NUS Graduate School, National University of Singapore, Singapore 119077, Singapore*

[2]*Department of Electrical and Computer Engineering, National University of Singapore, Singapore 117576, Singapore*

[3]*Institute of Materials Research & Engineering, Agency for Science, Technology & Research (A*STAR), Singapore 138634, Singapore*

[4]*Department of Physics, National University of Singapore, Singapore 117551, Singapore*

Electron-mediated spin torque provides a fast and efficient method to manipulate magnetization; however, electron motion inevitably brings about the generation of Joule heat and corresponding power consumption. Magnon-mediated spin torque, without involving moving electrons, could circumvent the energy dissipation issue. In this work, we fabricate a sandwich structure of topological insulator/antiferromagnetic insulator/ferromagnet with perpendicular magnetic anisotropy. We find that the magnon current with spin angular momentum can traverse a 25-nm-thick antiferromagnetic NiO layer and effectively switch the perpendicular magnetization of Co-Fe-B at room temperature with a critical switching current density of 4.1×10^6 A/cm^2. The magnon torque efficiency is characterized using spin-torque ferromagnetic resonance measurements to be 0.33 with a magnon diffusion length of 26.6 nm. Our work paves the way for manipulating perpendicular magnetization via magnon torques, facilitating the exploration of magnon-based spintronics with low power consumption.

I. INTRODUCTION

Spin-orbit torque (SOT) plays a pivotal role in spintronic devices because it provides an efficient and fast method to manipulate the magnetization of a ferromagnet [1–4]. In a SOT structure, the charge current flows in the spin source layer and generates a spin current due to spin-orbit interaction [5,6]. The spin current exerts torques on the adjacent ferromagnetic layer and enables the switching of the magnetization. Spin-orbit-torque-induced magnetization switching has been extensively studied because of its potential application in memory, logic, high-frequency devices, and neuromorphic computing [7–13]. However, electron-mediated spin torque, which involves moving charges, results in inevitable Joule heating and corresponding energy dissipation [4]. The issue can be circumvented by magnon-mediated spin torque involving magnon currents, where the spin angular momentum is carried by spin waves instead of moving electrons [14]. Therefore, magnon currents may enable Joule-heating-free transfer of spin angular momentums [15]. Moreover, magnon currents have a number of advantages compared with electron currents, such as their long diffusion length [16–18] and ultrafast propagation velocity [19]. Previously, antiferromagnetic magnon-driven switching was demonstrated based on a trilayer of topological insulator Bi$_2$Se$_3$/antiferromagnetic insulator NiO/ferromagnetic Ni-Fe [14]. However, Ni-Fe has a small in-plane anisotropy and can be easily influenced by external magnetic field disturbances, which significantly reduces the magnetic immunity of the device. Moreover, for high-density and fast-speed information storage, the switching of perpendicular magnetic anisotropy (PMA) is highly desirable, but technically challenging provided that constructing a PMA layer on top of such a magnon source layer is nontrivial. Very recently, magnon-mediated PMA switching was reported in all-oxide SrRuO$_3$/NiO/SrIrO$_3$ heterostructures at 60 K [20]. For practical application, room-temperature magnon-driven PMA switching is highly desirable.

In this work, we demonstrate antiferromagnetic magnon current-driven switching at room temperature in a sandwich heterostructure of Bi$_2$Te$_3$/NiO/Co-Fe-B, where the

---

ferromagnet Co-Fe-B exhibits PMA. The critical current density to switch the PMA is 4.1×10^6 A/cm^2, lower than or comparable to that for conventional electron-mediated systems [3,4,21–26]. Moreover, the magnon torque efficiency is determined to be 0.33 with a magnon diffusion length of 26.6 nm from spin-torque ferromagnetic resonance (ST-FMR) measurements.

II. RESULTS AND DISCUSSION

The experimental details are listed in the Supplemental Material [27]. We first use the ST-FMR technique [28,29] to quantify the magnon-mediated torque of Bi$_2$Te$_3$(8)/NiO(d)/Ni$_{81}$Fe$_{19}$(6)/SiO$_2$(2)/Ta(1.5) [Bi$_2$Te$_3$(8 nm)/NiO(d)/Py, numbers in parentheses are in

nanometers] samples, where NiO/Ni$_{81}$Fe$_{19}$/SiO$_2$/Ta is deposited in a magnetron sputtering chamber. The thickness of Bi$_2$Te$_3$ is chosen to be 8 nm, because Bi$_2$Te$_3$ exhibits the highest spin torque efficiency θ_{ST} at this thickness (Fig. S7 within the Supplemental Material [27]). The Py layer shows in-plane magnetic anisotropy, which is required for ST-FMR [28,29]. Figure 1(a) depicts a schematic diagram of the ST-FMR setup with the film stack structure. An in-plane radio-frequency current I_{rf} with frequencies f ranging from 7 to 12 GHz is applied along the x axis using a signal generator. The oscillating spin currents, which mainly originate from topological surface states [30–32], are generated in the Bi$_2$Te$_3$ layer and converted into a magnon current through the interfacial exchange interaction between Bi$_2$Te$_3$/NiO. The magnon
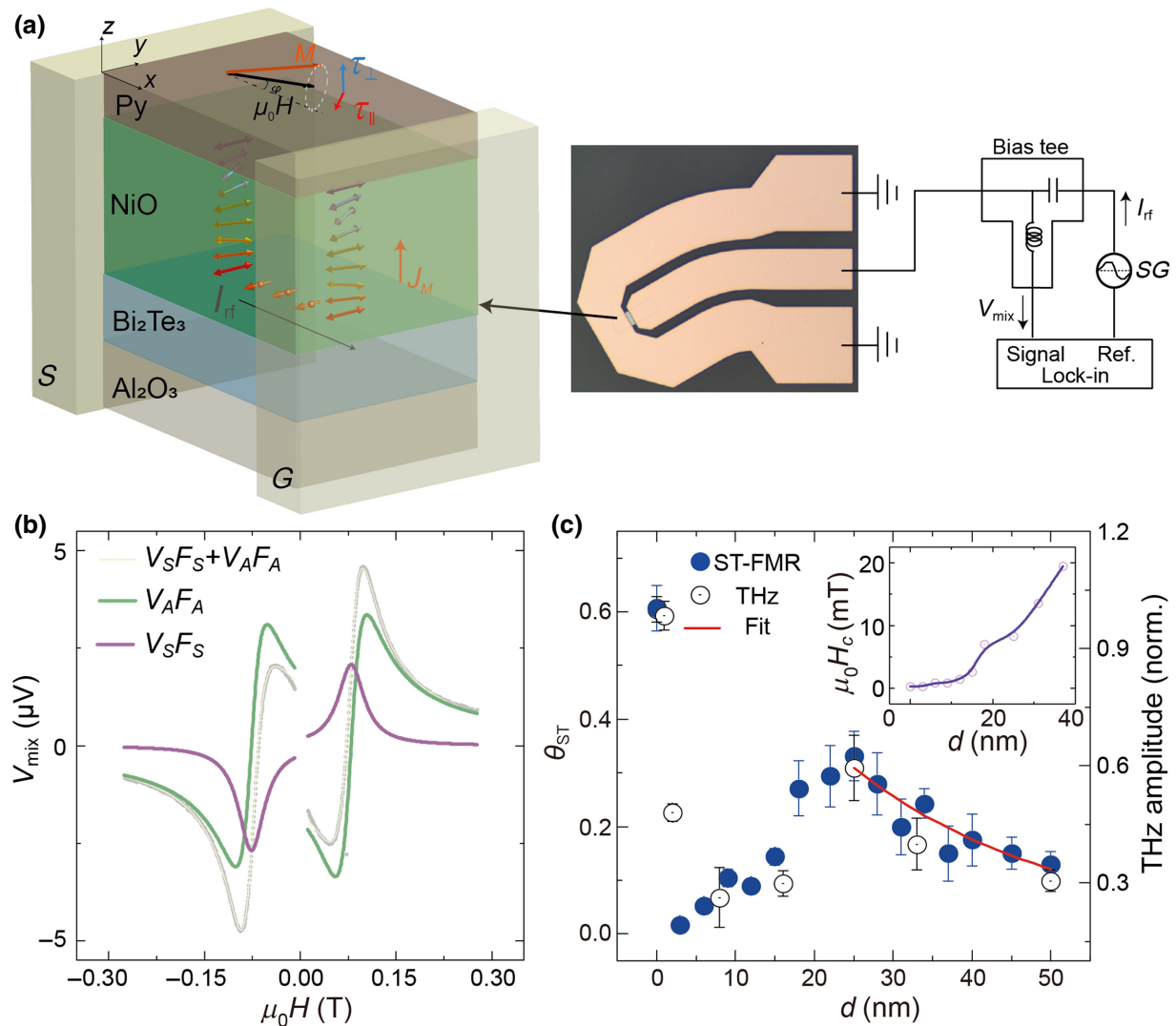

FIG. 1.   ST-FMR spectra from Bi$_2$Te$_3$/NiO(d)/Py. (a) Schematic diagram of the layer structure (left) and the measurement circuit connected to a ST-FMR device (right). (b) Typical ST-FMR signal of the Bi$_2$Te$_3$(8 nm)/NiO(25 nm)/Py device measured at 9 GHz. The solid lines are fits that show the symmetry ($V_S F_S$) (purple) and antisymmetry ($V_A F_A$) (green) Lorentzian contributions. (c) The spin torque efficiency θ_{ST}, the terahertz emission amplitude, and the coercivity $\mu_0 H_c$ of Py (inset) versus NiO thickness d. The red line is an exponential decay fitting of θ_{ST}.

currents pass through the NiO layer and exert oscillating magnon torques on the top Py layer including both the dampinglike torque $\gamma\tau_{DL}$ ($\mathbf{m} \times \boldsymbol{\sigma} \times \mathbf{m}$) and the fieldlike torque $\gamma\tau_{FL}$ ($\mathbf{m} \times \boldsymbol{\sigma}$), where $\mathbf{m}$ and $\boldsymbol{\sigma}$ are the unit vectors of the magnetization of Py and the induced magnon spin polarization from the NiO layer, respectively, and τ_{DL} and τ_{FL} are the dampinglike and fieldlike effective field induced by magnon or spin currents. Current I_{rf} also exerts an Oersted field torque $-\gamma(\mathbf{m} \times \mathbf{H_{Oe}})$ on the Py layer. These torques, which can be decomposed into the out-of-plane oriented torque $\tau_\perp$ and in-plane oriented torque $\tau_\parallel$, drive the magnetization of the Py layer away from equilibrium and into precession, thereby changing the anisotropic magnetoresistance of the Py layer. Consequently, the mixing of the change of the device resistance with I_{rf} gives rise to a dc voltage, which is measured as the ST-FMR signal V_{mix} by a lock-in amplifier (see Supplemental Material [27] for derivation of the ST-FMR mixing voltage). It is noteworthy that the propagation of I_{rf} along the Py layer has no impact on the results of the ST-FMR due to the absence of net torques in Py itself [28].

Figure 1(b) shows the typical ST-FMR signals from the Bi_2Te_3(8 nm)/NiO(25 nm)/Py sample measured at 9 GHz. The ST-FMR signal V_{mix} can be decomposed into two parts, $V_{mix} = V_S F_S + V_A F_A$, where $V_S F_S$ is the symmetric component contributed by the dampinglike torque and $V_A F_A$ is the antisymmetric component originating from the fieldlike torque as well as the Oersted-field-induced torque. The symmetric component indicates that the Py magnetization experiences a sizable dampinglike torque induced by magnon currents. It is noted that the amplitude of the symmetric component is not identical when the external field reverses. This is because the small out-of-plane component of the external field generates in-plane torque that contributes to the symmetric signal. This contribution can be excluded by averaging the amplitude of symmetric signals. Because the topological surface state may also contribute to the antisymmetric component of the ST-FMR signal, the ratio method for deriving the spin torque efficiency, which assumes that the antisymmetric component arises only from the Oersted-field-induced torque, might not be accurate for our system [14,30–32]. Therefore, we use only the symmetric component to evaluate the magnon torque efficiency θ_{ST} based on

$$V_S F_S = -\frac{I_{rf}\gamma\,\cos\varphi}{4}\frac{dR}{d\varphi}\tau_{DL}\frac{1}{\Delta}F_S, \quad (1)$$

$$\sigma_s = \frac{2e}{\hbar}\frac{\tau_{DL}M_s t_{Py}}{E}, \quad (2)$$

$$\theta_{ST} = \frac{\sigma_s}{\sigma}, \quad (3)$$

where γ is the gyromagnetic ratio, $\varphi = 40°$ is the external field direction with respect to the current I_{rf} direction, $dR/d\varphi$ is the angle-dependent magnetoresistance at

φ, $\Delta = 0.5\gamma\alpha(2\mu_0 H_{ext} + \mu_0 M_{eff})$ is the linewidth of the ST-FMR signal in the frequency spectrum, where α and M_{eff} are the damping constant and effective magnetization of Py, respectively, μ_0 is the vacuum permeability, σ_s is the spin Hall conductivity of spin source, M_s is the saturation magnetization of Py, which is determined to be 6.8×10^5 A/m using vibrating sample magnetometry (VSM), $t_{Py} = 6$ nm is the thickness of Py, σ is the electric conductivity of the spin source, and E is the microwave field applied to the device. From Eq. (1), we can obtain the dampinglike effective field τ_{DL} exerted on the Py magnetization, which is 7.6×10^{-3} mT. The microwave field E can be calculated by $E = j_{ss}/\sigma$, where j_{ss} is the microwave current density in the spin source (see Supplemental Material [27] for calculation of the microwave current density in Bi_2Te_3 and Py layers). Based on the calculated E and τ_{DL}, we determine θ_{ST} of the Bi_2Te_3(8 nm)/NiO(25 nm)/Py sample to be 0.33, comparable to or larger than that of electron-mediated spin torques [3,4,21–26].

Figure 1(c) summarizes the d dependence of θ_{ST} in Bi_2Te_3(8 nm)/NiO(d)/Py samples. The curve shows a typical antiferromagnetic-magnon-related behavior: a sharp decrease up to 3 nm, followed by a gradual increase, reaching a peak value as the NiO layer becomes thicker ($d \sim 25$ nm) [14,19]. The sudden decrease of θ_{ST} is ascribed to the blocking of the electron-mediated spin currents by the nonmagnetic NiO layer. This is evidenced by the lack of visible enhancement in the coercivity of the Py layer, as shown in the inset of Fig. 1(c) (see Fig. S9 within the Supplemental Material [27] for the hysteresis loops of Bi_2Te_3/NiO(d)/Py samples). With further increase of d, the coercivity of the Py layer gradually increases, indicating the formation of the antiferromagnetic ordering in the NiO layer [33], which is important for magnon transports in NiO [34,35]. Consequently, θ_{ST} increases due to the enhanced contribution of antiferromagnetic magnons and reaches a peak value at $d = 25$ nm. The exponential decay of θ_{ST} for $d > 25$ nm is due to the dominant spin angular momentum loss of antiferromagnetic magnons due to magnon-phonon relaxation [35]. By fitting the ST-FMR results of $d \geq 25$ nm using an exponential decay function $\theta_{ST} = \theta_0 \exp(-(d - d_0)/l_m)$, where l_m indicates the magnon diffusion length, the magnon diffusion length is determined to be 26.6 nm, which is comparable to a previous result with the Bi_2Se_3 underlayer [14]. In order to confirm the NiO thickness d dependence, we perform terahertz emission measurements, where the spin-to-charge conversion is characterized by the terahertz emission amplitude [36] on Bi_2Te_3(6 nm)/NiO(d)/$Ni_{81}Fe_{19}$(3 nm)/SiO_2(3 nm) samples. The terahertz emission amplitude reveals a trend similar to that of θ_{ST}, which verifies the observation of magnon torques.

We subsequently utilize magnon torques for efficient switching of a ferromagnetic layer with PMA. A film of Ti(2 nm)/$Co_{20}Fe_{60}B_{20}$(0.9 nm)/MgO(2 nm)/Ta(1.5 nm)
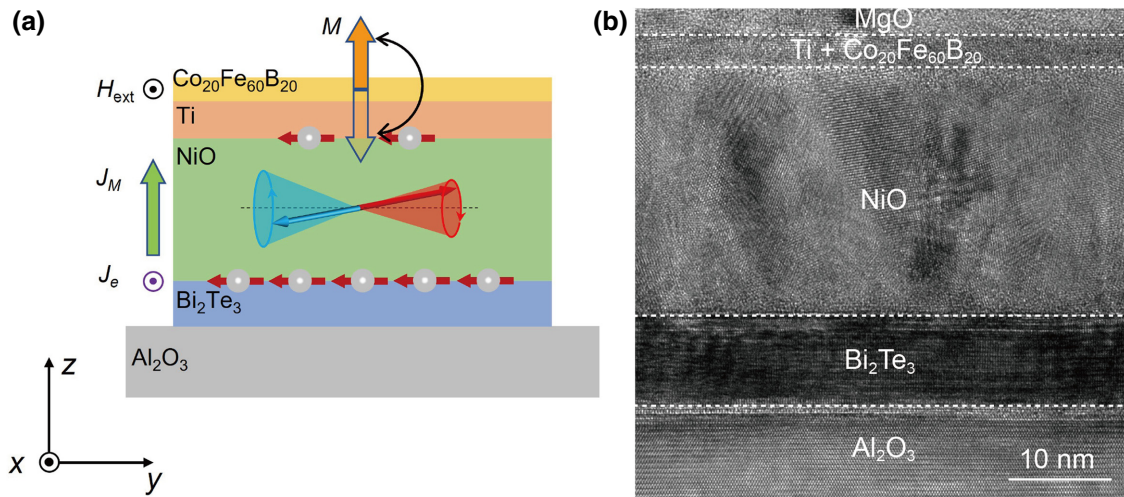
FIG. 2. Schematic of magnon-mediated spin-torque switching and sample characterization. (a) Schematic of magnon-induced switching of Co-Fe-B layer. The Co-Fe-B layer exhibits PMA. (b) High-resolution cross-sectional transmission electron microscopy image of Bi_2Te_3(8 nm)/NiO(25 nm)/Co-Fe-B, where the interfaces are indicated by the white dashed lines.

(Co-Fe-B) is deposited on top of Bi_2Te_3(8 nm)/NiO(25 nm) using magnetron sputtering. Here, we choose Ti as a buffer layer for the following two reasons. First, it has a negligible spin Hall angle and long spin diffusion length [23,37]. In the Bi_2Te_3/NiO/Co-Fe-B

Second, the Ti buffer layer can promote the formation of $Co_{20}Fe_{60}B_{20}$ perpendicular magnetization [37]. The saturation magnetization of $Co_{20}Fe_{60}B_{20}$ is measured to be 5.7×10^5 A/m by VSM. In the Bi_2Te_3/NiO/Co-Fe-B
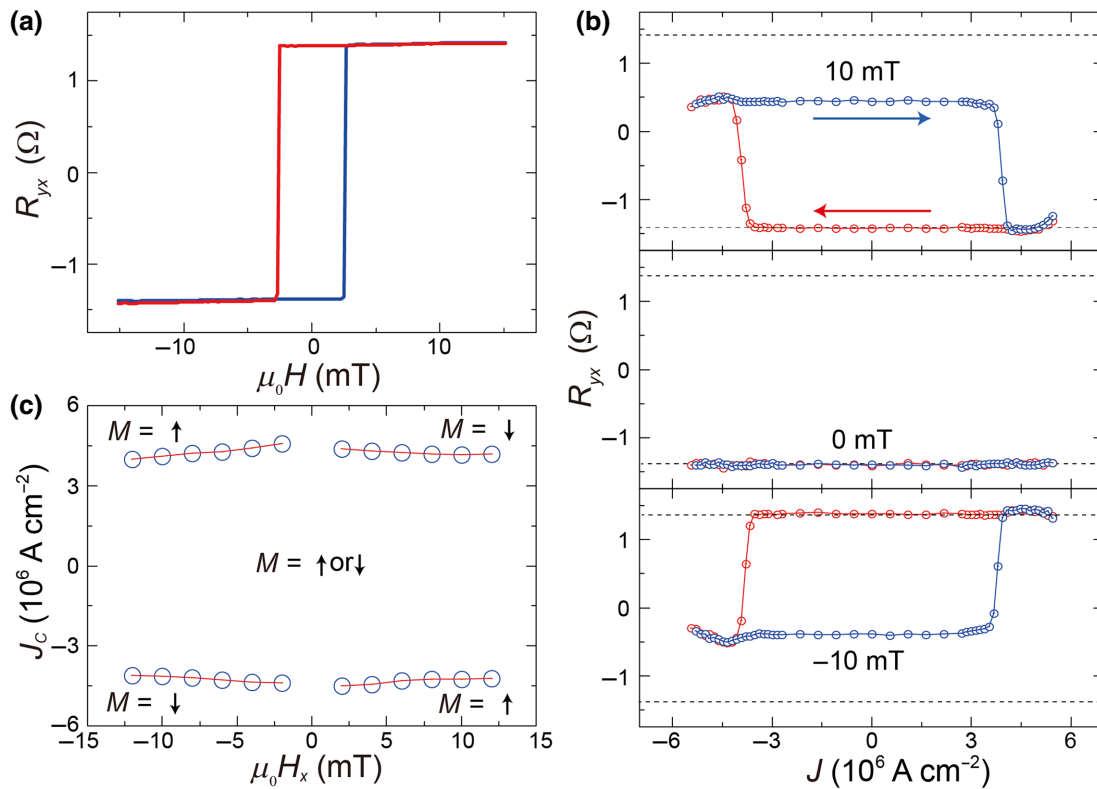

FIG. 3. Magnon-induced magnetization switching in the Bi_2Te_3(8 nm)/NiO(25 nm)/Co-Fe-B sample. (a) Anomalous Hall curve measured by sweeping the magnetic field ($\mu_0 H$) along the z direction. (b) Magnon-induced spin-torque switching under in-plane magnetic fields $\mu_0 H_x$ of -10, 0, and 10 mT. (c) $\mu_0 H_x$ dependence of critical switching current density J_C.

structure, an electric current in the surface of Bi_2Te_3 is spin polarized and generates nonequilibrium spin accumulation, whose direction is perpendicular to the electric current and parallel to the surface due to the spin-momentum locking effect. The nonequilibrium electron spin current in Bi_2Te_3 can convert into a magnon current in NiO through the interfacial exchange interaction. The magnon current then subsequently diffuses inside the NiO layer and exerts magnon torques on the top Co-Fe-B layer. The magnon torques drive the switching of the Co-Fe-B layer, as schematically shown in Fig. 2(a). Figure 2(b) shows a high-resolution transmission electron microscopy image of a typical Bi_2Te_3(8 nm)/NiO(25 nm)/Co-Fe-B sample. Clear and well-defined interfaces (marked by a dotted line) are observed not only at the Bi_2Te_3/NiO interface but also at the NiO/Co-Fe-B interface. The high-quality interfaces play an important role in the generation and propagation of magnon currents [38].

The film of Bi_2Te_3(8 nm)/NiO(25 nm)/Co-Fe-B is patterned into Hall bar devices with a width of $10\,\mu m$ and a length of $20\,\mu m$. The PMA of the Co-Fe-B layer is confirmed by the square-shaped anomalous Hall loop in Fig. 3(a). We note that no exchange bias is observed, which may result from the isolation of NiO and Co-Fe-B layer using Ti. To measure the magnon-induced magnetization switching, we inject a dc current pulse with $100-\mu s$ pulse width and different amplitudes to the Hall bar devices and probe the Hall voltage using a small dc current of 0.1 mA after each current pulse, under varying in-plane magnetic fields.

As shown in Fig. 3(b), a clear switching window is observed with an external field applied along the dc current pulse direction to break the symmetry, which indicates that the Co-Fe-B layer can be switched by magnon-mediated spin torques. The critical switching current density J_C in Bi_2Te_3 is 4.1×10^6 A/cm^2 (calculated by considering the parallel resistance model; see the Supplemental Material [27] for calculation of the current density in Bi_2Te_3 and PMA layers), smaller than or comparable to those of electron-mediated spin torques [3,4,21–26]. The switching is clockwise for a positive in-plane external field of 10 mT and anticlockwise for a negative external field of
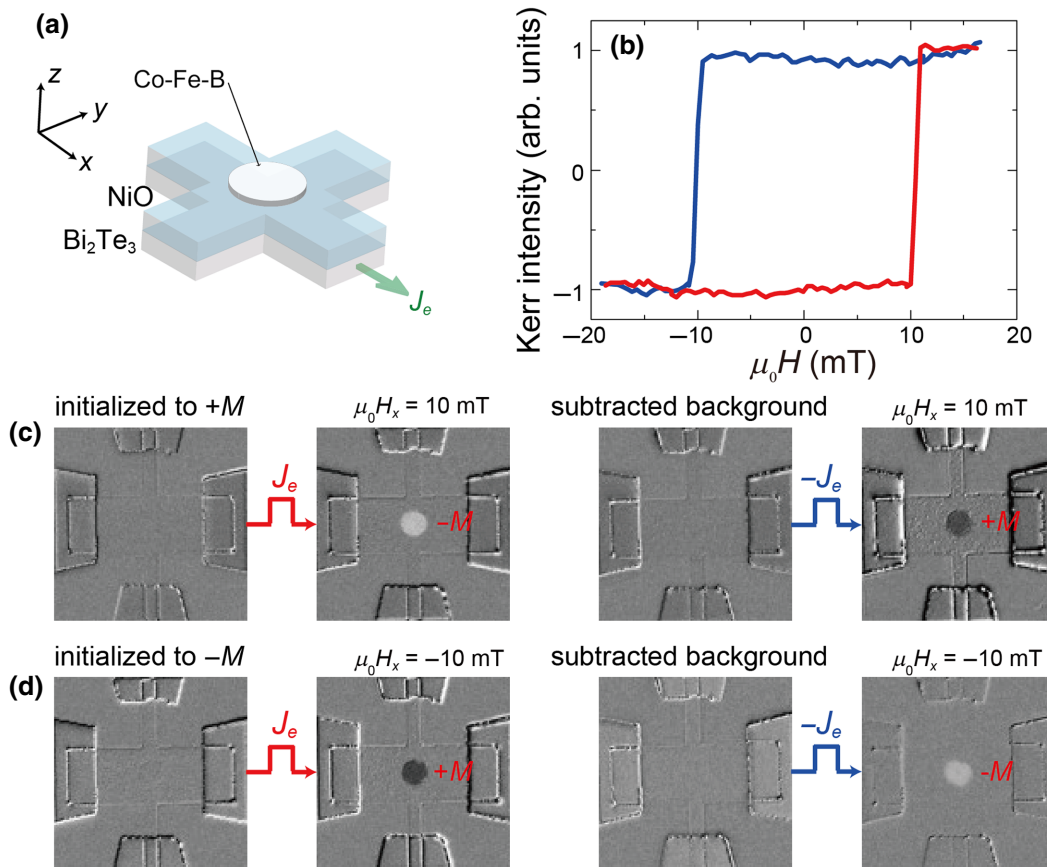

FIG. 4. Magnon-mediated spin-torque switching captured by MOKE. (a) Schematic of Co-Fe-B magnetic dot on top of Bi_2Te_3/NiO. (b) Hysteresis loop (μ_0H–M) measured by applying the magnetic field along the z direction. (c) MOKE images of switching the magnetization of Co-Fe-B magnetic dot by applying a pulse current along the x axis and with an external field of $\mu_0H_x = 10$ mT along the x direction. (d) MOKE images of Co-Fe-B magnetization switching with a current pulse along the x axis and $\mu_0H_x = -10$ mT. Black and white contrasts indicate the magnetization pointing up ($+M$) and down ($-M$), respectively.

−10 mT, which is similar to typical spin-torque-induced PMA switching behavior [2]. The switching loop is absent without the assisted external field, which indicates that magnon-torque-induced switching also requires an external magnetic field to break the symmetry [1,2]. Figure 3(c) shows the switching phase diagram, in which the critical current density slightly decreases with increasing external field. This behavior is similar to the case of electron-mediated switching [2]. We also carry out SOT switching measurements on Bi_2Te_3/Co-Fe-B samples, which show behavior similar to that of Bi_2Te_3/NiO/Co-Fe-B (Fig. S10 within the Supplemental Material [27]).

In order to further demonstrate the magnon-torque-induced switching and exclude the possible influence from current shunting into Ti/Co-Fe-B layers, the Co-Fe-B layer is patterned into magnetic dots with a radius of 5 μm in the center of a Hall bar cross as shown in Fig. 4(a). Polar magneto-optical Kerr effect (MOKE) microscopy is utilized to measure the Co-Fe-B switching. Before carrying out the switching measurement, we first measure the magnetic field $\mu_0 H$ dependence of the magnetization M to verify the PMA of the Co-Fe-B dot. As shown in Fig. 4(b), the square-shaped hysteresis loop demonstrates the retention of PMA after dot patterning. Figures 4(c) and 4(d) show the switching measurement results. We first initialize the magnetization of Co-Fe-B in the +z direction and subtract the background. Next, when a fixed magnetic field of 10 mT is applied along the +x direction to break the symmetry, the contrast of the Co-Fe-B dot turns white upon injecting an electrical current pulse with a current density of 5.7×10^6 A/cm^2 and a pulse width of 100 μs along the same direction, consistent with the switching of Co-Fe-B magnetization from the +z to −z direction. To enhance the contrast, we then subtract the background again and apply a current pulse of 6.2×10^6 A/cm^2 to the −x direction. This results in the contrast of the Co-Fe-B dot changing from white to black, indicating the down to up switching of the Co-Fe-B magnetization. The switching polarity is inverted on reversing the direction of the in-plane magnetic field, as shown in Fig. 4(d), and the Co-Fe-B magnetization favors pointing up (down) for positive (negative) current, which is consistent with the switching measurement results in Fig. 3(b). The imaged switching of the Co-Fe-B magnetic dots unambiguously demonstrates that the magnon-mediated spin torque can switch the electrically isolated Co-Fe-B dot with PMA.

III. CONCLUSION

We experimentally realize magnon-torque-driven switching of a ferromagnetic layer with PMA at room temperature. The critical switching current density using magnon torque is found to be as low as 4.1×10^6 A/cm^2 and the corresponding magnon torque efficiency is determined to be 0.33 with a magnon diffusion length of

26.6 nm. Finally, MOKE measurements exclude the possibility of artifacts contributed from buffer layers and show the magnon current can switch Co-Fe-B with PMA. We note that the magnon torques are excited by injecting electric current into the Bi_2Te_3 layer. However, we expect that our work will trigger pure magnon-driven magnetization switching without involving electric currents in the future.

[1] I. M. Miron, K. Garello, G. Gaudin, P.-J. Zermatten, M. V. Costache, S. Auffret, S. Bandiera, B. Rodmacq, A. Schuhl, and P. Gambardella, Perpendicular switching of a single ferromagnetic layer induced by in-plane current injection, Nature **476**, 189 (2011).

[2] L. Liu, C.-F. Pai, Y. Li, H. W. Tseng, D. C. Ralph, and R. A. Buhrman, Spin-torque switching with the giant spin hall effect of tantalum, Science **336**, 555 (2012).

[3] R. Ramaswamy, J. Lee, K. Cai, and H. Yang, Recent advances in spin-orbit torques: Moving towards device applications, Appl. Phys. Rev. **5**, 031107 (2018).

[4] Q. Shao, P. Li, L. Liu, H. Yang, S. Fukami, A. Razavi, H. Wu, F. Freimuth, Y. Mokrousov, M. D. Stiles, S. Emori, A. Hoffmann, J. Åkerman, K. Roy, J.-P. Wang, S.-H. Yang, K. Garello, and W. Zhang, Roadmap of spin–orbit torques, IEEE Trans. Magn. **57**, 1 (2021).

[5] A. Manchon, H. C. Koo, J. Nitta, S. M. Frolov, and R. A. Duine, New perspectives for Rashba spin-orbit coupling, Nat. Mater. **14**, 871 (2015).

[6] J. Sinova, S. O. Valenzuela, J. Wunderlich, C. H. Back, and T. Jungwirth, Spin Hall effects, Rev. Mod. Phys. **87**, 1213 (2015).

[7] S. Emori, U. Bauer, S.-M. Ahn, E. Martinez, and G. S. Beach, Current-driven dynamics of chiral ferromagnetic domain walls, Nat. Mater. **12**, 611 (2013).

[8] K. Garello, F. Yasin, S. Couet, L. Souriau, J. Swerts, S. Rao, S. Van Beek, W. Kim, E. Liu, S. Kundu, D. Tsvetanova, N. Jossart, K. Croes, E. Grimaldi, M. Baumgartner, D. Crotti, A. Furnemont, P. Gambardella, and G. S. Kar, in *IEEE Symp. VLSI Circuits* (2018), p. 81.

[9] V. E. Demidov, S. Urazhdin, H. Ulrichs, V. Tiberkevich, A. Slavin, D. Baither, G. Schmitz, and S. O. Demokritov, Magnetic nano-oscillator driven by pure spin current, Nat. Mater. **11**, 1028 (2012).

[10] Z. Luo, A. Hrabec, T. P. Dao, G. Sala, S. Finizio, J. Feng, S. Mayr, J. Raabe, P. Gambardella, and L. J. Heyderman, Current-driven magnetic domain-wall logic, Nature **579**, 214 (2020).

[11] A. Kurenkov, S. DuttaGupta, C. Zhang, S. Fukami, Y. Horio, and H. Ohno, Artificial neuron and synapse realized in an antiferromagnet/ferromagnet heterostructure using

dynamics of spin-orbit torque switching, Adv. Mater. **31,** 1900636 (2019).

[12] A. Manchon, J. Železný, I. M. Miron, T. Jungwirth, J. Sinova, A. Thiaville, K. Garello, and P. Gambardella, Current-induced spin-orbit torques in ferromagnetic and antiferromagnetic systems, Rev. Mod. Phys. **91,** 035004 (2019).

[13] X. Qiu, Z. Shi, W. Fan, S. Zhou, and H. Yang, Characterization and manipulation of spin orbit torque in magnetic heterostructures, Adv. Mater. **30,** 1705699 (2018).

[14] Y. Wang, D. Zhu, Y. Yang, K. Lee, R. Mishra, G. Go, S.-H. Oh, D.-H. Kim, K. Cai, E. Liu, S. D. Pollard, S. Shi, J. Lee, K. L. Teo, Y. Wu, K.-J. Lee, and H. Yang, Magnetization switching by magnon-mediated spin torque through an antiferromagnetic insulator, Science **366,** 1125 (2019).

[15] A. V. Chumak, V. I. Vasyuchka, A. A. Serga, and B. Hillebrands, Magnon spintronics, Nat. Phys. **11,** 453 (2015).

[16] Y. Kajiwara, K. Harii, S. Takahashi, J. Ohe, K. Uchida, M. Mizuguchi, H. Umezawa, H. Kawai, K. Ando, K. Takanashi, S. Maekawa, and E. Saitoh, Transmission of electrical signals by spin-wave interconversion in a magnetic insulator, Nature **464,** 262 (2010).

[17] L. J. Cornelissen, J. Liu, R. A. Duine, J. Ben Youssef, and B. J. van Wees, Long-distance transport of magnon spin information in a magnetic insulator at room temperature, Nat. Phys. **11,** 1022 (2015).

[18] R. Lebrun, A. Ross, S. A. Bender, A. Qaiumzadeh, L. Baldrati, J. Cramer, A. Brataas, R. A. Duine, and M. Kläui, Tunable long-distance spin transport in a crystalline antiferromagnetic iron oxide, Nature **561,** 222 (2018).

[19] K. Lee, D.-K. Lee, D. Yang, R. Mishra, D.-J. Kim, S. Liu, Q. Xiong, S. K. Kim, K.-J. Lee, and H. Yang, Superluminal-like magnon propagation in antiferromagnetic NiO at nanoscale distances, Nat. Nanotechnol. **16,** 1337 (2021).

[20] D. Zheng, J. Lan, B. Fang, Y. Li, C. Liu, J. O. Ledesma-Martin, Y. Wen, P. Li, C. Zhang, Y. Ma, Z. Qiu, K. Liu, A. Manchon, and X. Zhang, High-efficiency magnon-mediated magnetization switching in all-oxide heterostructures with perpendicular magnetic anisotropy, Adv. Mater. **34,** 2203038 (2022).

[21] C.-F. Pai, L. Liu, Y. Li, H. W. Tseng, D. C. Ralph, and R. A. Buhrman, Spin transfer torque devices utilizing the giant spin Hall effect of tungsten, Appl. Phys. Lett. **101,** 122404 (2012).

[22] S. Fukami, C. L. Zhang, S. DuttaGupta, A. Kurenkov, and H. Ohno, Magnetization switching by spin–orbit torque in an antiferromagnet–ferromagnet bilayer system, Nat. Mater. **15,** 535 (2016).

[23] Y.-W. Oh, S.-H. C. Baek, Y. M. Kim, H. Y. Lee, K. Lee, C. Yang, E. Park, K. Lee, K. Kim, G. Go, J. Jeong, B. Min, H.-W. Lee, K.-J. Lee, and B.-G. Park, Field-free switching of perpendicular magnetization through spin–orbit torque in antiferromagnet/ferromagnet/oxide structures, Nat. Nanotechnol. **11,** 878 (2016).

[24] J. H. Han, A. Richardella, S. A. Siddiqui, J. Finley, N. Samarth, and L. Q. Liu, Room-Temperature Spin-Orbit Torque Switching Induced by a Topological Insulator, Phys. Rev. Lett. **119,** 077702 (2017).

[25] Y. Wang, P. Deorani, X. Qiu, J. H. Kwon, and H. Yang, Determination of intrinsic spin Hall angle in Pt, Appl. Phys. Lett. **105,** 152412 (2014).

[26] X. Qiu, P. Deorani, K. Narayanapillai, K.-S. Lee, K.-J. Lee, H.-W. Lee, and H. Yang, Angular and temperature dependence of current induced spin-orbit effective fields in Ta/CoFeB/MgO nanowires, Sci. Rep. **4,** 4491 (2014).

[27] See Supplemental Material at http://link.aps.org/supplemental/10.1103/PhysRevApplied.19.034039 for experimental section, derivation of ST-FMR mixing voltage equation, calculation of current density in ST-FMR and switching measurements, characterizations of Bi_2Te_3 and Bi_2Te_3/NiO films on sapphire, transport results of Bi_2Te_3 films, ST-FMR results of Bi_2Te_3/Py samples, VSM results of Bi_2Te_3/NiO/Py samples, and SOT switching of Bi_2Te_3(8 nm)/Co-Fe-B and Bi_2Te_3(11 nm)/NiO(25 nm)/Co-Fe-B.

[28] L. Q. Liu, T. Moriyama, D. C. Ralph, and R. A. Buhrman, Spin-Torque Ferromagnetic Resonance Induced by the Spin Hall Effect, Phys. Rev. Lett. **106,** 036601 (2011).

[29] D. Fang, H. Kurebayashi, J. Wunderlich, K. Výborný, L. P. Zârbo, R. P. Campion, A. Casiraghi, B. L. Gallagher, T. Jungwirth, and A. J. Ferguson, Spin-orbit-driven ferromagnetic resonance, Nat. Nanotechnol. **6,** 413 (2011).

[30] A. R. Mellnik, J. S. Lee, A. Richardella, J. L. Grab, P. J. Mintun, M. H. Fischer, A. Vaezi, A. Manchon, E. A. Kim, N. Samarth, and D. C. Ralph, Spin-transfer torque generated by a topological insulator, Nature **511,** 449 (2014).

[31] Y. Wang, P. Deorani, K. Banerjee, N. Koirala, M. Brahlek, S. Oh, and H. Yang, Topological Surface States Originated Spin-Orbit Torques in Bi_2Se_3, Phys. Rev. Lett. **114,** 257202 (2015).

[32] Y. Wang, D. P. Zhu, Y. Wu, Y. M. Yang, J. W. Yu, R. Ramaswamy, R. Mishra, S. Y. Shi, M. Elyasi, K. L. Teo, Y. H. Wu, and H. Yang, Room temperature magnetization switching in topological insulator-ferromagnet heterostructures by spin-orbit torques, Nat. Commun. **8,** 1364 (2017).

[33] J. Nogués and I. K. Schuller, Exchange bias, J. Magn. Magn. Mater. **192,** 203 (1999).

[34] H. Wang, C. Du, P. C. Hammel, and F. Yang, Antiferromagnonic Spin Transport from $Y_3Fe_5O_{12}$ into NiO, Phys. Rev. Lett. **113,** 097202 (2014).

[35] S. M. Rezende, R. L. Rodríguez-Suárez, and A. Azevedo, Diffusive magnonic spin transport in antiferromagnetic insulators, Phys. Rev. B **93** 054412 (2016).

[36] Y. Wu, M. Elyasi, X. Qiu, M. Chen, Y. Liu, L. Ke, and H. Yang, High-performance THz emitters based on ferromagnetic/nonmagnetic heterostructures, Adv. Mater. **29,** 1603031 (2017).

[37] H. Wu, P. Zhang, P. Deng, Q. Lan, Q. Pan, S. A. Razavi, X. Che, L. Huang, B. Dai, K. Wong, X. Han, and K. L. Wang, Room-Temperature Spin-Orbit Torque from Topological Surface States, Phys. Rev. Lett. **123,** 207205 (2019).

[38] Y. Cheng, K. Chen, and S. Zhang, Giant magneto-spin-Seebeck effect and magnon transfer torques in insulating spin valves, Appl. Phys. Lett. **112,** 052405 (2018).